PHYSICAL REVIEW D VOLUME 35, NUMBER 9 1 MAY 1987

Measurement of $\bar{p}p$ elastic scattering at beam momenta between 390 and 780 MeV/c

T. Kageyama,[*] T. Fujii,[†] K. Nakamura,[*] F. Sai, S. Sakamoto,[‡] S. Sato,[§]
T. Takahashi, T. Tanimori,[*] and S. S. Yamamoto
Department of Physics, University of Tokyo, Tokyo 113, Japan

Y. Takada
Institute of Applied Physics, University of Tsukuba, Sakura, Ibaraki 305, Japan

(Received 16 May 1986)

The differential cross sections of $\bar{p}p$ elastic scattering have been measured at incident beam momenta of 390, 490, 590, 690, and 780 MeV/c. The results are compared with the predictions of various $\bar{N}N$ potential models. None of these models completely explains the present results.

I. INTRODUCTION

At low energies, the antinucleon-nucleon ($\bar{N}N$) interactions are described by $\bar{N}N$ potentials. However, our present understanding of the $\bar{N}N$ interactions is by no means complete. Although the long-range part of the real $\bar{N}N$ potential is known from the well-understood nucleon-nucleon (NN) potentials by applying the "G-parity transformation," the short-range part of the real potential and the entire imaginary potential are not very well known.

Some phenomenological $\bar{N}N$ potential models have been proposed so far.[1–5] All these models introduced a set of free parameters which were determined by fitting the available $\bar{N}N$ scattering data. There are other approaches to construct the $\bar{N}N$ potential with a minimum number of parameters with the aid of underlying physical pictures. These include the boundary-condition model[6] and some models based on the quark-gluon picture of hadrons.[7–14]

In order to critically examine or to improve these models, more $\bar{N}N$ scattering data with good quality are needed. However, high-statistics data were only reported by Eisenhandler *et al.*[15] above 690 MeV/c and by Brückner *et al.*[16] between 180 and 600 MeV/c. Other data at low momenta exist,[17,18] but their quality is not high enough to test theoretical models critically.

In this experiment, we have measured the $\bar{p}p$ differential cross sections at 390, 490, 590, 690, and 780 MeV/c (Ref. 19), together with the differential cross sections of the charge-exchange reaction $\bar{p}p \to \bar{n}n$.[20] At the same time, we have measured the differential cross sections of the reactions $\bar{p}p \to \pi^+\pi^-$ and K^+K^- (Ref. 21). Here we report the results of the measurement of $\bar{p}p$ elastic scattering. We then compare our results with the predictions of some theoretical models, some of which have been previously quoted in our publication of the $\bar{p}p$ charge-exchange results.[20]

In addition to the $\bar{p}p$ elastic-scattering results, we present the numerical values of our $\bar{p}p \to \bar{n}n$ differential-cross-section results in the Appendix, because, while these results are very often used together with the elastic-scattering data in theoretical analyses, the numerical values of our $\bar{p}p \to \bar{n}n$ results have not been published yet.

II. EXPERIMENTAL

A. Apparatus

The experiment was conducted with the low-momentum separated beam channel K3 at the 12-GeV proton synchrotron of the National Laboratory for High Energy Physics (KEK), using the apparatus shown in Fig. 1.

The antiproton beam was defined by three trigger counters $C1$ (not shown in Fig. 1), $C2$, and $C3$, and its trajectory was determined by two multiwire proportional chambers with bidimensional readout (MWPC1 and MWPC2) and a cylindrical drift chamber (CDC).[22] The beam intensity per 10^{12} primary protons of 12 GeV/c impinging on a 40-mm-long platinum target was about 200 $\bar{p}$'s at 590 MeV/c, decreasing to about 35 $\bar{p}$'s at 390 MeV/c. The $\pi^-/\bar{p}$ ratio was about 100 at 590 MeV/c,

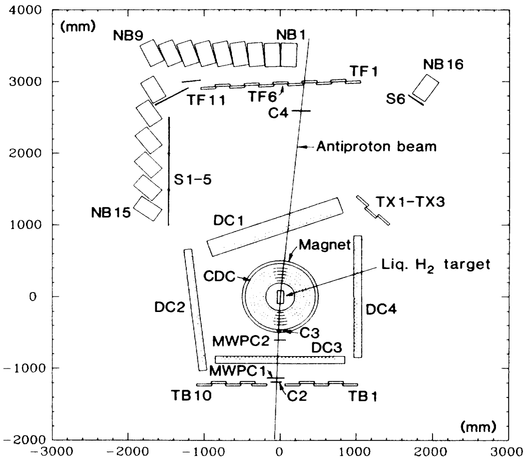

FIG. 1. Experimental arrangement. $C2-C4$, trigger counters; MWPC1 and MWPC2, multiwire proportional chambers of bidimensional readout; CDC, five-layer cylindrical drift chamber; DC1—DC4, four-layer planar drift chambers; TF1—TF11, TB1—TB10, and TX1—TX3, time-of-flight counters; NB1—NB16, iron-scintillator sandwich counters; $S1-S6$, scintillation counters.

increasing to 700 at 390 MeV/c. The absolute accuracy of the beam momentum estimated from the known properties of the K3 beam-channel magnets was ±0.5%. We independently checked that the beam momentum was correct to within ±2%, using the kinematical constraint of the two-body reactions $\bar{p}p \rightarrow \pi^+\pi^-$ and K^+K^-, which were measured concurrently with elastic and charge-exchange channels. The momentum spread of the beam was ±2.5%.

A 17.5-cm-long liquid-hydrogen target cell with a diameter of 8 cm was made of 250-μm-thick Mylar. The target cell had a double-cylinder structure; namely, inside the target cell a 76-μm-thick concentric Mylar cylinder was placed for screening bubbles created on the inner surface of the target cell, thus making the density correction due to boiling of liquid hydrogen negligible.[23] The temperature of liquid hydrogen was controlled to within ±0.14 K, and the effective density of liquid hydrogen obtained from the average vapor pressure (1.079 kg/cm^2) was 0.0706±0.0002 g/cm^2.

The liquid-hydrogen target was located at the center of the CDC. The target and the CDC were placed in a C-type dipole magnet. The magnet had circular pole pieces with a diameter of 100 cm, and the gap of the pole pieces was 60 cm. The applied magnetic field was 2.5 kG at the center of the magnet. The magnetic field was mapped with use of a three-dimensional Hall probe prior to setting up the experimental equipment, and was fitted to a smooth function. On the surface of the magnet pole pieces were attached thin scintillation counters called the pole-face counters (not shown in Fig. 1) in order to detect charged annihilation products.

The drift cells of the CDC were arranged in five equally spaced concentric layers: the radius of the inner-most layer was 22 cm and that of the outer-most one was 39.6 cm. There were two types of drift cells with different cell sizes. The small cells with a maximum drift distance of 0.864 cm were employed for the CDC region where the beam traversed, so as to prevent the loss of efficiency due to the intense charged-particle flux. For the other CDC region, the large drift cells with a maximum drift distance of 1.728 cm were employed. The height of the active CDC volume was 30 cm. The CDC covered about 20% of 4π solid angle around the target. All sense wires of the CDC were perpendicular to the reaction plane, and therefore the CDC provided charged-particle trajectories projected onto that plane.

Outside the magnetic field were located four planar drift chambers, DC1—DC4. Of these, only DC1 was relevant to the measurement of $\bar{p}p$ elastic scattering. Each of DC1—DC4 had four layers of drift cells, providing two horizontal and two vertical coordinates of charged-particle tracks. The cell size was common to DC1—DC4, having a maximum drift distance of 1.2 cm. Two horizontal layers of each planar drift chamber were staggered with each other by a half cell size in order to resolve the left-right ambiguity. Two vertical layers had the same structure. Since DC1 measured the tracks of low-momentum protons and antiprotons, it was gas-sealed by thin Mylar sheets glued to the G10 frame. The other planar drift chambers had relatively thick walls made of acrylic foam sandwiched by thin G10 boards.

Downstream of the target, there was a circular scintillation counter $C4$ used to veto those events in which the incident antiprotons passed through the target without interaction, or else they were scattered in the extreme forward direction. A 20-cm-diam. scintillator was used at 780 and 690 MeV/c as $C4$, while a 30-cm-diam. scintillator was used at lower momenta. Because the magnetic field of the magnet was fixed, the beam orbit changed with the incident momentum. Also the size of the beam after having traversed the target changed with the incident momentum because of the different amount of multiple Coulomb scattering. Therefore, the position of the counter $C4$ was adjusted each time the beam momentum was changed so as to keep the veto efficiency approximately constant.

In the forward and backward directions, two walls of time-of-flight (TOF) counters, TF and TB, were located. These TOF counters were primarily used to identify pions and kaons in the analysis of the $\bar{p}p \rightarrow \pi^+\pi^-$ and K^+K^- reactions. For the analysis of elastic scattering, the forward TOF counter wall TF, consisting of 11 scintillators TF1—TF11, each having a width of 20 cm, a height of 150 cm, and a thickness of 3 cm, also provided identification of protons and antiprotons (charges were known from the drift-chamber data). Each TOF counter element was viewed by two high-gain, low-noise photomultipliers, Hamamatsu R1332. Test results[24] indicated that these TOF counters had an intrinsic rms time resolution of about 150 psec. The overall time resolution including the resolution of the TOF start counter $C2$ and the ambiguity of the reaction point in the target due to the finite position resolution of the drift chambers, was about 200 psec. The performance of the TOF counters was periodically checked during the experiment by a laser-based monitoring system.[25] The other detectors are not relevant to the measurement of elastic scattering, and are described elsewhere.[19,20]

B. Trigger

Since the present experiment was planned to measure the reactions $\bar{p}p \rightarrow \pi^+\pi^-$, K^+K^-, $\bar{p}p$, and $\bar{n}n$ concurrently, the trigger scheme was required to cause no bias for all the measured reactions. We adopted a very simple trigger scheme with which almost all the $\bar{p}p$ interaction events were recorded. Namely, except at 390 MeV/c the events were triggered by $(C1 \cdot C2 \cdot C3)_{\bar{p}} \cdot \overline{C4}$, where $(C1 \cdot C2 \cdot C3)_{\bar{p}}$ represents the incident beam defined by the coincidence of the counters $C1$, $C2$, and $C3$, timed to the antiprotons, and $\overline{C4}$ eliminated the noninteracting events. With this trigger requirement, however, there still remained a substantial amount of triggers due to pions contaminating the beam. This was caused by high counting rate of the counter $C1$ which was located near the electrostatic separator of the K3 beam channel. The residual pion triggers were reduced by adjusting the attenuation factors of the trigger counter signals from $C1$, $C2$, and $C3$. The pulse heights of these trigger counters for the minimum-ionizing particles were adjusted below the discriminator threshold. With this technique, the ratio of the pion beam contamination in the trigger decreased to less than 15% at all the beam momenta.

With the requirement $\overline{C4}$, about 75% of the incident-antiproton events were suppressed and the remaining 25% of the incident-antiproton events were recorded. Our loose trigger requirement did not cause significant dead-time loss because of the low intensity of the antiproton beam. On the average it was about 260 $\bar{p}$'s per 0.5 sec of beam burst at 590 MeV/c (corresponding to 1.3×10^{12} primary protons), and was even lower at 390 MeV/c (40 $\bar{p}$'s per beam burst, corresponding to 1.1×10^{12} primary protons). Therefore at 390 MeV/c, all the incident $\bar{p}$ events including noninteracting events were recorded with a trigger $(C1\cdot C2\cdot C3)_{\bar{p}}$. This trigger mode was free from any bias, and therefore it was also used at other momenta for a small fraction of data taking for the purpose of making various kinds of checks.

Because of the loose triggers, a great amount of unnecessary events, most of which were caused by $\bar{p}p$ annihilation into multipions, were recorded in addition to useful events. Most of the unnecessary events were easily eliminated later in the off-line analysis by using the information from the pole-face counters. It should be noted that the pole-face counters were not used at the trigger level for eliminating multipion annihilation events, because they would also eliminate backward elastic-scattering events whose back-scattered low-momentum antiprotons will annihilate in the target.

C. Experimental procedure

The data taking was sequentially performed from the highest to the lowest momentum. Prior to data taking at each momentum, we carefully tuned the beam momentum and beam phase space. The beam momentum was so adjusted as to obtain the quoted values of 390, 490, 590, 690, and 780 MeV/c at the center of the liquid-hydrogen target, taking the energy loss of the beam into account. Also, as already described the position of the counter $C4$ was adjusted prior to data taking at each momentum.

Data were collected by a PDP-11/34 on-line computer through a CAMAC system and were recorded on magnetic tape. In parallel with the data acquisition, part of the data was subjected to the on-line analysis in order to monitor the performance of the detectors. Furthermore, during the experiment the recorded data were checked in detail in the off-line analysis using the KEK central computer M200H.

In addition to the data-taking runs, some special runs were performed. (i) The laser calibration runs for the TOF counters were performed once a day. (ii) Empty-target runs were performed at each beam momentum in order to estimate the effect from the walls of the target cell. (iii) Some runs were performed with the magnetic field off, in order to determine the precise positions of the drift chambers and multiwire proportional chambers. (iv) Some data were taken with the pion beam trigger for checking the detector response to minimum-ionizing particles.

III. ANALYSIS

A. Outline of analysis

Although the charged particles emerging from the target passed through the magnet, the momentum resolution was poor because of the low magnetic field (2.5 kG) and short path length inside the magnet. Consequently, the magnet only served to determine the charge of the outgoing particles. The elastic-scattering events were selected with two different methods depending on the scattering angle.

In the forward and backward regions in the center-of-mass frame, the forward TOF counters TF6—TF11 were used to identify the antiprotons or protons with the use of the timing information. (We did not use TF1—TF5 to avoid possible biases caused by scattering or absorption caused either by the support or light guide of the counter $C4$ or by one of the supporting rods of the target vacuum chamber.) The forward-going particle was required to pass through DC1. In these kinematical regions, either the proton or antiproton scattered at an angle θ (scattering angle in the center-of-mass frame) near 180° has too low a momentum in the laboratory frame to emerge from the target, and therefore it cannot be detected. We call these elastic-scattering events the one-prong events.

In the intermediate angular region, two charged tracks of the scattered antiproton and recoil proton can be seen in the CDC. One of the two outgoing particles was required to be detected by DC1. We call these events the two-prong events. Unambiguous identification of the protons or antiprotons using the TOF counters was not possible in most of this angular region. The selection of the two-prong elastic-scattering events was done by using the opening angle.

There is a limited angular region where one of the outgoing particles in the two-prong event can be identified by the TOF counter TF11. Using the events falling into this category, we checked the consistency between the two methods used to select the elastic-scattering events.

B. Identification of antiprotons in the beam

As described in Sec. II B, the incident antiprotons were tightly selected by the trigger logic. However, because of the high counting rate of $C1$, part of the recorded events were due to beam pions which caused the accidental $(C1\cdot C2\cdot C3)_{\bar{p}}$ signal.

These accidental pion events were rejected in the off-line analysis, using both pulse-height and timing information of the trigger counters $C2$ and $C3$. In order to determine the rejection criteria, pure samples of both beam pions and antiprotons were needed. These were selected by using one of the TF counters, which was hit by the beam. As shown in Fig. 2, the beam pions and antiprotons were clearly separated in the two-dimensional plot of TOF versus pulse height. Using the pure samples selected on this plot the cuts on the distributions of the pulse height and timing of the counters $C2$ and $C3$ were determined to reject beam pions.

The purity of the incident antiprotons selected by the above method could be inspected by using the TOF versus pulse-height distribution of the TOF counter for the selected events. By sacrificing about 1—15% of incident antiprotons, depending on the beam momentum, the antiprotons in the beam were purified to better than 99% at all momenta.

C. Reconstruction of charged tracks

In the horizontal plane, charged-particle tracks were reconstructed with the use of the quintic spline fitting method.[26] For the reconstruction of a charged-particle track projected onto the horizontal plane, the CDC was required to have more than three hit layers along the trajectory. The track-finding procedure in the CDC was based on the link and tree method developed by the TASSO group.[27] In addition, both MWPC1 and MWPC2 were required to have a unique horizontal hit coordinate for the incident-beam track, and DC1 was required to have at least one horizontal hit coordinate for the outgoing track passing through it.

If the incoming track and the outgoing track passing through DC1 were successfully reconstructed, they were extrapolated inward assuming circular orbits in order to determine the vertex point in the horizontal plane. Figure 3 shows the distribution of the vertex points in the horizontal plane, where the profile of the liquid-hydrogen target is clearly seen.

The vertical coordinate of the incident-beam track was provided by MWPC1 and MWPC2. Taking these vertical coordinates into account, three-dimensional spline fitting was performed, and the vertical coordinate of the vertex point was determined. For the spatial reconstruction of the outgoing track passing through DC1, two vertical layers of DC1 were required to have hits. Three-dimensional spline fitting of the outgoing track was then performed, using the previously determined vertex point.

The two-prong event had another outgoing track whose coordinates were provided by only the CDC. This track was reconstructed only in the horizontal plane, because kinematically it had to pass through the region between DC1 and DC4, and had no vertical-coordinate information. In the horizontal-plane reconstruction, this track was constrained to originate from the previously determined vertex point.

D. Event selection

To select elastic-scattering events in the one-prong region (i.e., the forward and backward directions) the following criteria were imposed on the data.

(a) At least one of the TF6—TF11 counters should have a signal consistent with the timing and pulse height of $\bar{p}$ or p.

(b) The reconstructed outgoing track should intersect the TF counter having the $\bar{p}$ (or p) signal. If there are two or more reconstructed outgoing tracks, one of these should satisfy the above requirement.

(c) A vertex point should exist in the target.

To select the elastic-scattering events in the two-prong region the following criteria were imposed on the data.

(i) Two charged-particle trajectories should exist in the CDC in addition to the incident antiproton, and one of them should pass through DC1.

(ii) A vertex point should exist in the target.

(iii) There should be no pole-face-counter hits.

(iv) The angles of the two outgoing tracks projected

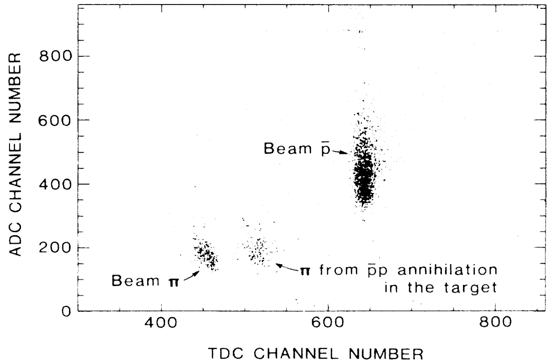

FIG. 2. An example of the scatter plot of time of flight vs pulse height obtained from one of the TF counters, which was hit by the beam. Events mostly cluster in the three regions corresponding to the beam antiprotons, beam pions, and pions originating from the $\bar{p}p$ annihilation reactions in the liquid-hydrogen target.

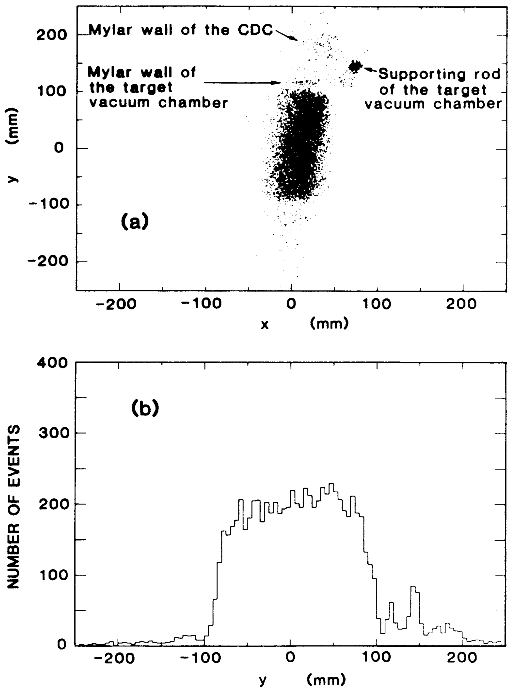

FIG. 3. (a) The vertex-point distribution for the one-prong events, projected onto the horizontal (x-y) plane. Besides the profile of the liquid-hydrogen target, other interaction sources such as the Mylar wall of the CDC, Mylar wall and the supporting rod of the target vacuum chamber can be recognized. (b) The vertex-point distribution projected onto the y axis.

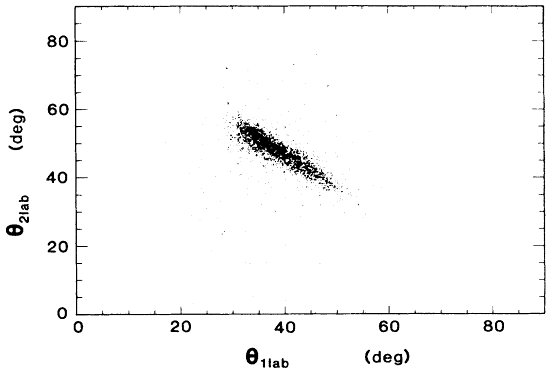

FIG. 4. Scatter plot showing the angle correlation for the two-prong events. The abscissa (ordinate) is the laboratory angle of the charged-particle track going to the left (right) with respect to the beam direction.

onto the horizontal plane should be consistent with the kinematics of $\bar{p}p$ elastic scattering.

Although one of the outgoing tracks passing through DC1 was reconstructed three dimensionally, the other outgoing track was reconstructed only in the horizontal plane. Hence, in criterion (iv) the consistency was checked in the horizontal plane. However, because of the limited acceptance in the vertical direction, there is not much difference between the true opening angle of the two outgoing tracks of the elastic event and the opening angle of the same tracks projected onto the horizontal plane. Figure 4 shows a scatter plot of the angles of the two outgoing tracks selected with criteria (i)—(iii). A strong correlation due to the $\bar{p}p$ elastic-scattering events is seen. Figure 5 shows a distribution of the difference between the measured angle of the track going to the right with respect to the beam direction and the angle predicted for this track from the elastic-scattering kinematics, assuming that the scattering took place in the horizontal plane. A smooth background seen in Fig. 5 is due to annihilation events. The residual background under the elastic peak was less than 1%, and was subtracted from it.

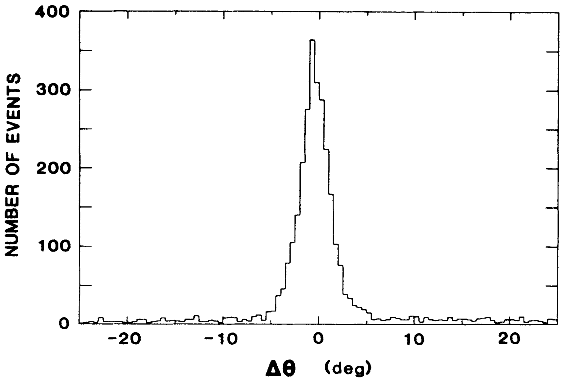

FIG. 5. Distribution of the difference $\Delta\theta$ between the measured angle of the track going to the right with respect to the beam direction and the angle predicted for this track from the measured angle of the left-going track, assuming the $\bar{p}p$ elastic-scattering kinematics. It was also assumed that the scattering took place in the horizontal plane.

E. Reconstruction efficiencies

The track-reconstruction efficiencies were independently estimated for the incoming antiprotons, for the scattered antiprotons or recoil protons in the one-prong events, and for both outgoing particles in the two-prong events.

The reconstruction efficiency for the incident antiprotons was determined at each beam momentum as the probability that the track passing through the trigger counters *C*1, *C*2, and *C*3 was reconstructed, using a sample of events selected by the beam-antiproton requirement. The resulting efficiency is about 70% with a typical statistical error of ±0.2%.

The angular dependence of the track-reconstruction efficiency for the outgoing antiprotons or protons in the kinematical region corresponding to the one-prong events was estimated by using the antiprotons or protons identified by the TF counters. The angular dependence mainly resulted from the requirement on the vertex reconstruction, whose efficiency depended on the angle between the incident and outgoing tracks. The angle-averaged track-reconstruction efficiency for the one-prong events ranged from 70% to 81% depending on the beam momentum with an estimated contribution of ±2% to the systematic normalization error.

For the two-prong events, it was not possible to identify definitely the scattered antiproton and recoil proton in most of the kinematical region corresponding to the two-prong events. Only TF11 could be used to identify either antiproton or proton hitting it. Consequently, we selected a sample of events satisfying the following conditions for the two-prong events: (i) TF11 should have a signal with the timing consistent with the scattered antiproton or recoil proton; (ii) two charged-track candidates should be found in the CDC in addition to the incident antiproton track. The results of the reconstruction efficiency ranged from 53% to 69% depending on the beam momentum. The angular dependence of the track-reconstruction efficiency could not be determined with this method. From the angular dependence of the track-reconstruction efficiency for the one-prong events, we estimate that this introduced a contribution of about ±4% to the systematic normalization error.

F. Acceptance and absorption correction

The Monte Carlo method was used to calculate the geometrical acceptance of the apparatus. The $\bar{p}p$ elastic-scattering events were generated isotropically, and the same event-selection criteria as used for the analysis of the actual events were imposed on the simulated events. Thus, the geometrical acceptance was separately calculated for the one-prong events and the two-prong events.

In this Monte Carlo simulation, the following effects were taken into account: (i) the incident-beam phase space at the liquid-hydrogen target; (ii) the energy loss of the beam in liquid hydrogen; (iii) the energy loss and multiple scattering of the outgoing particle(s); and (iv) the nuclear absorption of the outgoing particle(s) in liquid hydrogen and in other materials.

The simulated outgoing particle was traced by using the Runge-Kutta method with a small step. At each step the energy loss, the multiple-scattering angle, and the probability of surviving nuclear absorption were calculated.

The estimation of the absorption corrections due to liquid hydrogen for the incident and scattered antiprotons was made with two different methods. In one method the $\bar{p}p$ annihilation cross section σ_A given by Lowenstein *et al.*,[28]

$$\sigma_A = 36.5 + 28.9/p \text{ (mb)} ,$$

was used, where p is the beam momentum in units of GeV/c. In the other method, the $\bar{p}p$ absorption cross section $\sigma_{\text{abs}}(\bar{p}p)$ given by Loken and Derrick,[29]

$$\sigma_{\text{abs}}(\bar{p}p) = \pi(a + \hbar c/k)^2 ,$$

was used, where $a = 0.87$ fm and k is the center-of-mass momentum. The latter cross section $\sigma_{\text{abs}}(\bar{p}p)$ resulted in larger absorption corrections, but the difference between the correction factors calculated with σ_A and $\sigma_{\text{abs}}(\bar{p}p)$ is not very large. The final correction was made with $\sigma_{\text{abs}}(\bar{p}p)$, taking into account the difference between the correction factor using σ_A and that using $\sigma_{\text{abs}}(\bar{p}p)$ as a systematic error.

For the absorption corrections for the scattered antiprotons due to the materials between the target and the detectors, the nuclear antiproton-absorption cross sections reported by Nakamura *et al.*[30] were used. The correction factor obtained was (1±0.5)% at all incident beam momenta.

Figure 6 shows a typical acceptance function including the effects of the absorption correction and multiple scattering.

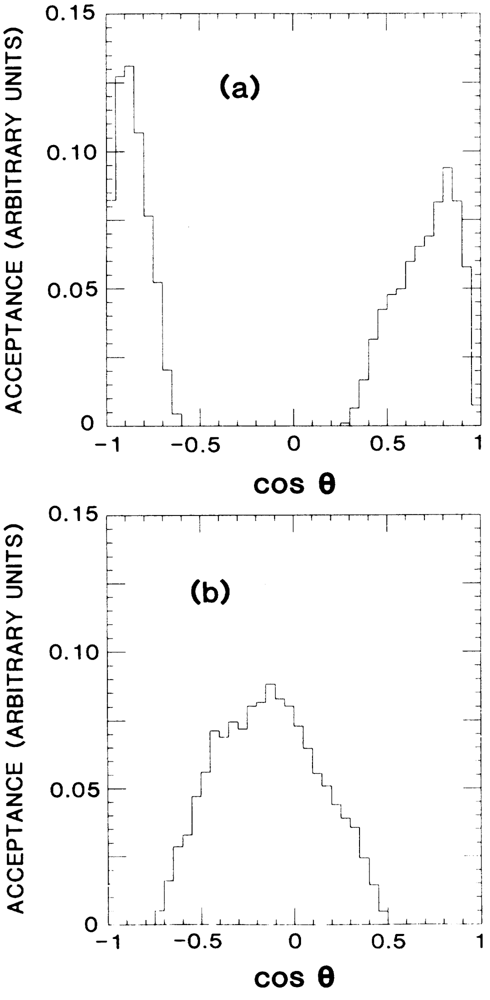

FIG. 6. Acceptances for (a) the one-prong events and for (b) the two-prong events, both at 490 MeV/c.

G. Subtraction of the empty-target contribution

To estimate the background contribution from the Mylar walls of the liquid-hydrogen target, empty-target runs were performed. Figure 7 shows the vertex-point distribution in a typical empty-target run. The angle-integrated contribution from the Mylar walls was found to be 5–6.5 % of the full-target contribution.

The background events from the Mylar walls contaminated mostly the one-prong events, because only the negligibly small hydrogen content of Mylar gave the two-prong contribution which could not be distinguished from $\bar{p}p$ elastic-scattering events from liquid hydrogen. This

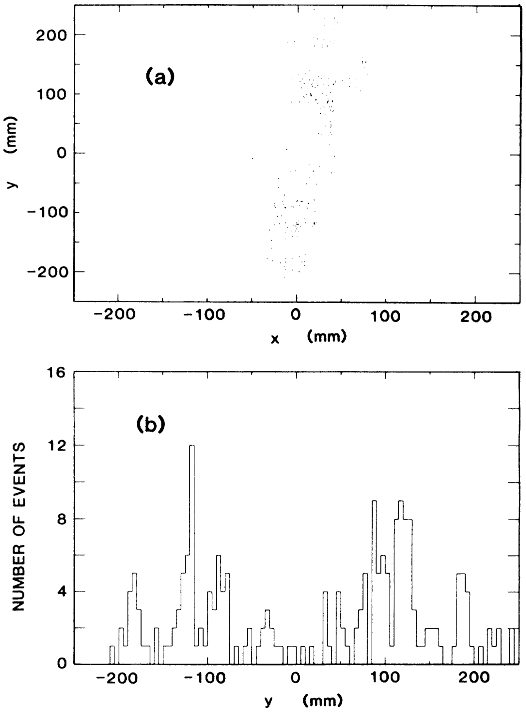

FIG. 7. (a) The vertex-point distribution for the one-prong events projected onto the horizontal (x-y) plane in the empty-target run. (b) The vertex-point distribution projected onto the y axis.

fact is indeed observed in Fig. 8, which shows the angular distribution of the events having the vertex point at the Mylar wall of the CDC, selected with the same criteria for the elastic events having the vertex point in the target. The forward peak is due to antiproton elastic scattering by nuclei, while the backward peak is due to proton emission following antiproton annihilation in nuclei, which is theoretically predicted[31-34] and experimentally observed.[35] The actual subtraction of the background was performed on the basis of the observed angular distributions of the antiprotons and protons from the antiproton interactions with Mylar.

H. Normalization

Events were triggered by $(C1\cdot C2\cdot C3)_{\bar{p}}\cdot\overline{C4}$, except at 390 MeV/$c$. Although the rate $(C1\cdot C2\cdot C3)_{\bar{p}}$ properly vetoed by the computer dead time was counted by a scaler, this could not be directly used for the beam normalization, because pions contaminated $(C1\cdot C2\cdot C3)_{\bar{p}}$ at the trigger level, and the beam cuts were imposed on the timing and pulse-height data from the trigger counters for the selection of antiprotons in the off-line analysis.

To obtain the number of incident antiprotons corresponding to the data retained after the beam cuts, we analyzed the data taken with the $(C1\cdot C2\cdot C3)_{\bar{p}}$ trigger, which was intermittently used during data taking with the main trigger $(C1\cdot C2\cdot C3)_{\bar{p}}\cdot\overline{C4}$. After applying the same beam cut as applied to the data taken with the main trigger mode, we obtained the ratio of the number of events satisfying the condition of the main trigger mode to the number of incident antiprotons. At each beam momentum, this ratio was found to be constant to within ±2% for the data taken with the $(C1\cdot C2\cdot C3)_{\bar{p}}$ trigger at different times.

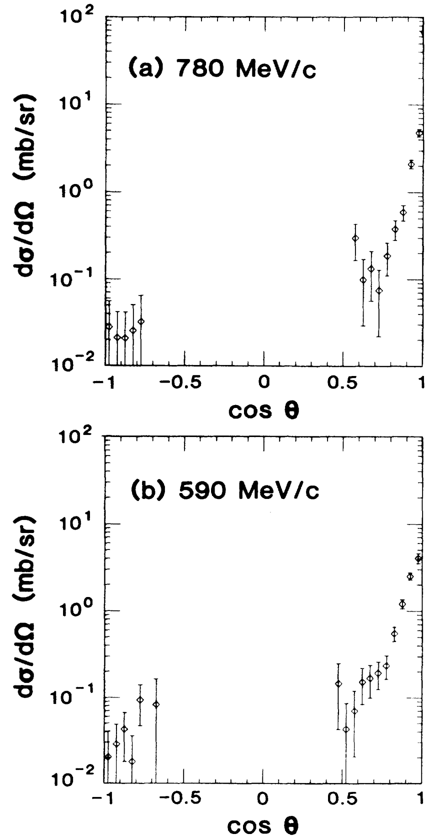

FIG. 8. Angular distributions of the one-prong events having the vertex point at the Mylar wall of the CDC at (a) 780 MeV/c and (b) 590 MeV/c. These distributions are normalized to the subtracted background cross sections.

The number of target protons depends on the length and density (0.0706±0.0002 g/cm^2) of the liquid-hydrogen target. The effective length of the target with spherically shaped Mylar end caps was determined as the mean value of the path lengths of incident antiprotons through the target, assuming that they had traversed the target without interacting with it. For this purpose, the reconstructed trajectory of the incident antiproton was extrapolated to the downstream end of the target by using the Runge-Kutta method. A typical uncertainty of the effective target length was ±2%.

I. Other corrections and summary of systematic errors

There are some other corrections which have not been discussed yet. One is the correction for the trigger suppression caused by the accidental or genuine hit in $C4$ in coincidence with the $(C1\cdot C2\cdot C3)_{\bar{p}}$ signal; the latter was due to the charged particles originating from the annihilation of elastically scattered antiprotons. The correction factors were estimated by inspecting the data taken in the $(C1\cdot C2\cdot C3)_{\bar{p}}$ trigger mode to be (0.5±0.5)% independent of the beam momentum and the scattering angle.

The other corrections are concerned with the two-prong events only. First, in the analysis of the two-prong events, we required the existence of two charged-particle tracks in addition to the incident antiproton track in the CDC. Therefore, if the incident antiproton was accompanied by another charged-particle within the sensitive time of the CDC, that event was rejected. The percentage of the incident antiproton track being accompanied by another charged-particle track was estimated to be (7±3)% at all beam momenta by visually inspecting the event display. Second, we also required the condition of the absence of a hit in the pole-face counter for the two-prong events. By inspecting the data taken in the $(C1\cdot C2\cdot C3)_{\bar{p}}$ trigger mode, we estimate that (1±0.5)% of the two-prong events were rejected by this requirement due to the accidental hit in the pole-face counter.

The dominant systematic errors are summarized in Table I. Added in quadrature, the total systematic error of the differential cross sections is typically ±5% for the one-prong events and ±7% for the two-prong events.

IV. RESULTS AND DISCUSSION

A. Experimental results

Figure 9 shows the $\bar{p}p$ elastic differential cross sections thus obtained. The error bars represent the statistical errors only. The forward and backward data points shown by the diamonds represent the differential cross sections

TABLE I. Summary of the systematic errors.

	One-prong events	Two-prong events
Beam normalization	±2%	±2%
Effective target length	±2%	±2%
Track reconstruction	±2%	±4%
Absorption correction	±1.5%	±2%
Acceptance	±3%	±3%
Loss of events due to the accompanying charged track		±3%
Accidental hits in the pole-face counters		±0.5%
Trigger suppression due to the *C*4 hit by the $\bar{p}$ annihilation products or due to the accidental *C*4 hit	±0.5%	±0.5%
Added in quadrature	±5%	±7%

determined by using the one-prong events, while the data points shown by the squares represent the differential cross sections determined by the two-prong events. The numerical values are given in Table II. At 390 MeV/*c*, the momenta of the outgoing antiproton and proton in the two-prong events became too low to make reliable absorption corrections, and therefore only the differential cross sections determined from the one-prong events are shown. At the other momenta, there are some regions where the differential cross sections could be determined by using both one-prong and two-prong events. The differential cross sections determined from the two different types of events are found to be consistent to within the quadratic sum of the statistical and systematic errors. An example

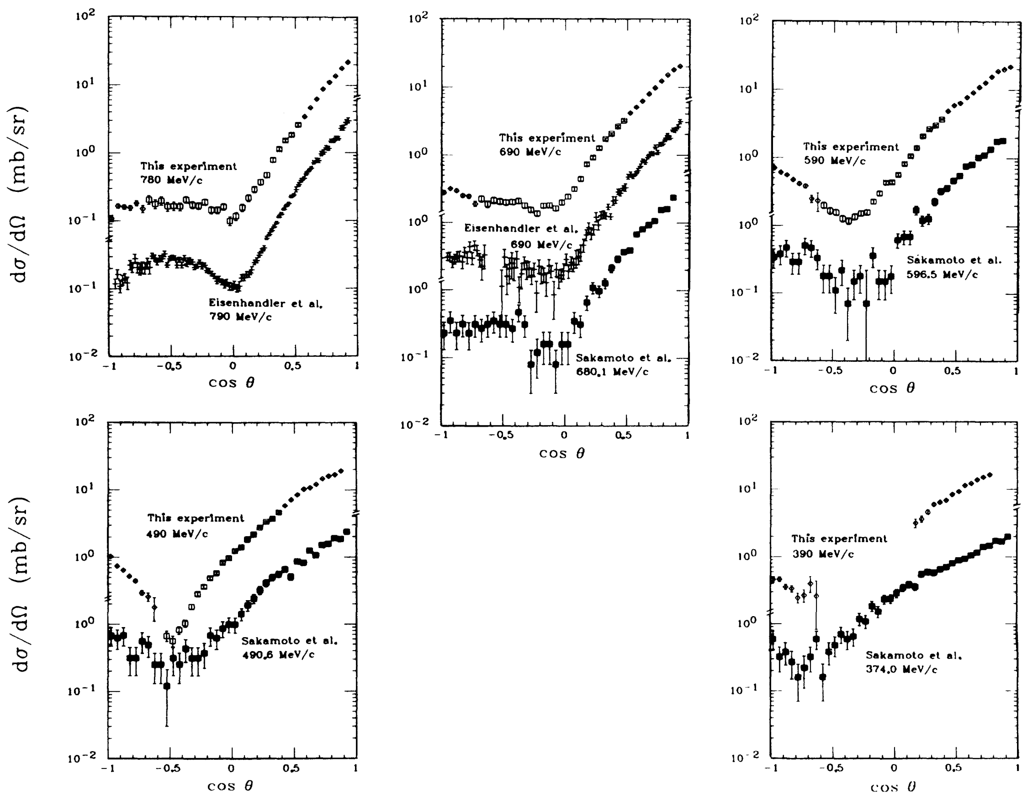

FIG. 9. $\bar{p}p$ elastic differential-cross-section results compared with those of Eisenhandler *et al.* (Ref. 15) and Sakamoto *et al.* (Ref. 18). The open diamonds show our data in the one-prong region. The open squares show our data in the two-prong region. The pluses show the data of Eisenhandler *et al.* (Ref. 15) and the solid squares show the data of Sakamoto *et al.* (Ref. 18).

TABLE II. Differential-cross-section results for $\bar{p}p$ elastic scattering.

$\cos\theta$ \ Beam momentum (MeV/c)	392.4±16.7 (390)	490.1±10.8 (490)	591.2±8.6 (590)	689.0±7.8 (690)	780.5±7.9 (780)
0.925			21.9±0.2	20.4±0.1	21.9±0.2
0.875		19.2±0.2	20.1±0.1	18.1±0.1	17.8±0.1
0.825		16.9±0.1	18.9±0.1	15.2±0.1	13.7±0.1
0.775	16.4±0.3	16.1±0.1	15.6±0.1	12.4±0.1	11.1±0.1
0.725	15.0±0.3	14.7±0.1	12.9±0.1	9.9±0.1	8.8±0.1
0.675	13.9±0.3	12.2±0.1	11.0±0.1	8.0±0.1	6.3±0.1
0.625	12.2±0.3	10.8±0.1	9.1±0.1	6.3±0.1	4.7±0.1
0.575	11.3±0.3	10.3±0.1	7.8±0.1	5.1±0.1	3.5±0.1
0.525	9.2±0.3	8.5±0.1	6.5±0.1	4.2±0.1	2.6±0.1
0.475	8.4±0.3	7.2±0.1	6.0±0.1	3.2±0.1	1.88±0.09
0.425	6.9±0.3	5.9±0.1	4.9±0.2	2.7±0.1	1.56±0.08
0.375	6.5±0.3	4.7±0.2	3.7±0.1	2.1±0.1	1.16±0.07
0.325	6.0±0.3	3.8±0.1	3.0±0.1	1.73±0.07	0.80±0.06
0.275	4.6±0.3	3.4±0.1	2.7±0.1	1.28±0.06	0.48±0.04
0.225		2.8±0.1	2.1±0.1	0.92±0.05	0.38±0.04
0.175		2.2±0.1	1.41±0.06	0.74±0.04	0.29±0.03
0.125		1.84±0.06	1.07±0.05	0.45±0.03	0.22±0.03
0.075		1.43±0.05	0.82±0.04	0.32±0.02	0.16±0.02
0.025		1.26±0.04	0.57±0.03	0.25±0.02	0.12±0.02
−0.025		0.98±0.04	0.44±0.03	0.20±0.02	0.10±0.02
−0.075		0.84±0.03	0.44±0.03	0.16±0.02	0.16±0.02
−0.125		0.59±0.03	0.30±0.02	0.18±0.02	0.15±0.02
−0.175		0.49±0.03	0.23±0.02	0.18±0.02	0.15±0.02
−0.225		0.37±0.02	0.16±0.01	0.14±0.01	0.19±0.02
−0.275		0.28±0.02	0.15±0.01	0.16±0.02	0.17±0.02
−0.325		0.18±0.02	0.14±0.01	0.18±0.02	0.17±0.02
−0.375		0.10±0.01	0.12±0.01	0.21±0.02	0.20±0.02
−0.425		0.08±0.01	0.13±0.01	0.20±0.02	0.16±0.02
−0.475		0.06±0.01	0.16±0.02	0.20±0.02	0.17±0.02
−0.525		0.07±0.01	0.17±0.02	0.21±0.02	0.16±0.02
−0.575			0.20±0.02	0.21±0.02	0.20±0.03
−0.625	0.26±0.18	0.18±0.07	0.23±0.07	0.19±0.02	0.18±0.03
−0.675	0.40±0.11	0.26±0.04	0.25±0.03	0.23±0.03	0.21±0.03
−0.725	0.26±0.06	0.30±0.02	0.38±0.03	0.19±0.02	0.15±0.02
−0.775	0.24±0.04	0.44±0.02	0.42±0.02	0.25±0.02	0.18±0.02
−0.825	0.34±0.04	0.52±0.02	0.48±0.02	0.25±0.01	0.15±0.01
−0.875	0.36±0.03	0.64±0.02	0.55±0.02	0.29±0.01	0.16±0.01
−0.925	0.46±0.04	0.74±0.02	0.61±0.02	0.32±0.01	0.16±0.01
−0.975	0.46±0.04	1.03±0.03	0.70±0.03	0.28±0.01	0.11±0.01

is shown in Fig. 10.

Our results at 780 and 690 MeV/c are compared with those of Eisenhandler *et al.*[15] at 790 and 690 MeV/c. Both data agree within the statistical uncertainties, except for possible discrepancies around $\cos\theta \sim -0.5$ at 780 MeV/c and in the forward region ($\cos\theta \lesssim 0.2$) at both 780 and 690 MeV/c. In the forward region, our data tend to be smaller than those of Eisenhandler *et al.*[15] by 10–20%. This discrepancy seems too large to be explained by the claimed normalization uncertainties of ±5% for the present experiment (one-prong region) and ±4% for the experiment of Eisenhandler *et al.*[15]

TABLE III. Legendre-expansion coefficients (mb/sr).

Beam momentum (MeV/c)	a_0	a_1	a_2	a_3	a_4	a_5	a_6
390	5.43±0.18	10.34±0.25	7.25±0.28	1.76±0.45	−0.34±0.53	−0.31±0.24	
490	4.93±0.02	9.73±0.04	7.92±0.06	2.52±0.07	0.37±0.06	−0.22±0.04	
590	4.54±0.01	9.48±0.03	8.72±0.04	3.95±0.05	0.84±0.06	−0.23±0.05	−0.20±0.03
690	3.57±0.01	7.92±0.03	8.13±0.03	5.05±0.04	1.97±0.05	0.38±0.04	0.01±0.03
780	3.21±0.01	7.56±0.03	8.51±0.04	6.43±0.05	3.34±0.05	1.17±0.04	0.22±0.03

Our data are also compared with those of Sakamoto *et al.*[18] Both data are in agreement except for a possible discrepancy at 490 MeV/c around $\cos\theta \sim -0.5$.

We have fitted our data to a Legendre-polynomial series of up to the sixth order at 780, 690, and 590 MeV/c, and up to the fifth order at the other momenta. The resulting expansion coefficients are given in Table III. Figure 11 shows the ratios of the coefficients a_i/a_0 for $i=1-5$ as functions of incident momentum together with those reported by Eisenhandler *et al.*[15] and by Sakamoto *et al.*[18] The behavior of our results is in agreement with those of the previous results.

The total elastic cross section is given as $4\pi a_0$, where a_0 is the coefficient of the zeroth Legendre polynomial and is given in Table III. The results are shown in Fig. 12 together with some previous data.[17,18,36,37] Here, an error of ±5% is assigned to our data considering the normalization uncertainty. As can be seen from this figure, our data at 690 and 780 MeV/c are lower ($\sim$20%) than the results of Coupland *et al.*,[37] which were deduced by using mainly the elastic differential-cross-section data of Eisenhandler *et al.*[15] This agrees with the behavior of our forward elastic differential cross sections as compared with that of Eisenhandler *et al.*[15] because the large diffraction peak of the $\bar{p}p$ forward elastic differential cross section contributes to the total elastic cross section most significantly.

From the results of the Legendre-expansion fit to our data, the elastic differential cross section at $\theta = 180°$ can be deduced. Clearly, the results obtained with this approach depend on the order of Legendre polynomial fit. Therefore we assigned an error of ±10% to the results obtained by using the expansion coefficients given in Table

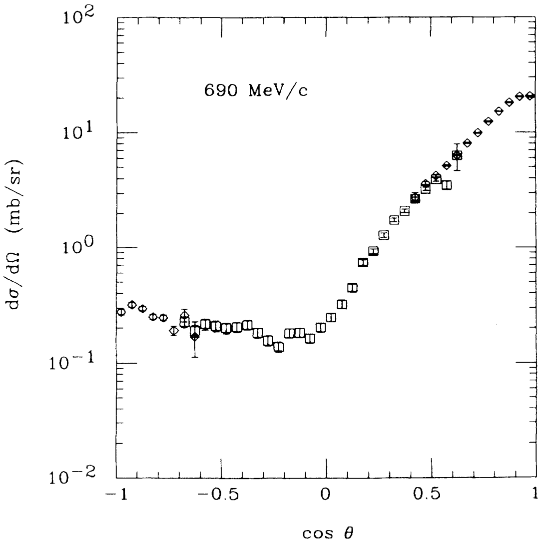

FIG. 10. At 690 MeV/c, the data in the overlap region between the one-prong and two-prong regions are explicitly shown. The open diamonds show the $\bar{p}p$ elastic differential cross sections determined from the one-prong events and the open squares show those determined from the two-prong events.

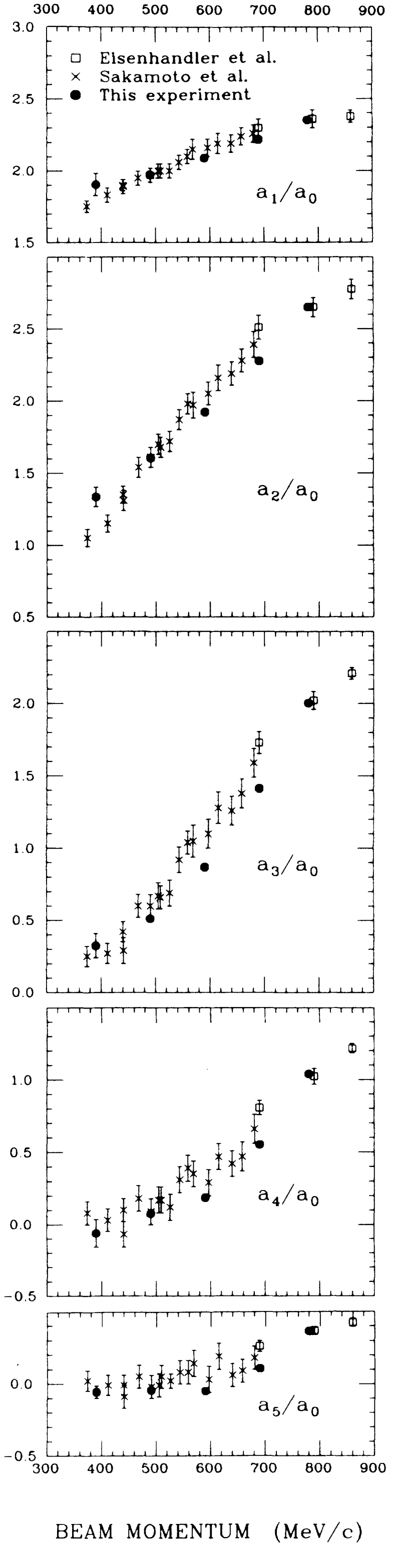

FIG. 11. Legendre coefficients obtained by the fit to the $\bar{p}p$ elastic differential-cross-section data. Our results (solid circles) are compared with the results of Eisenhandler *et al.* (Ref. 15) (open squares) and Sakamoto *et al.* (Ref. 18) (crosses).

TABLE IV. The results of the $\bar{p}p \to \bar{n}n$ reaction reported in Ref. 20.

Beam momentum (MeV/c)	392.4±16.7		490.1±10.8		591.2±8.6		689.0±7.8		780.5±7.9	
Systematic error (%)		8.1		8.5		9.3		9.1		8.7
	$\cos\theta$	$d\sigma/d\Omega$	$\cos\theta$	$d\sigma/d\Omega$	$\cos\theta$	$d\sigma/d\Omega$	$\cos\theta$	$d\sigma/d\Omega$	$\cos\theta$	$d\sigma/d\Omega$
Differential cross section (mb/sr)	0.985	2.41±0.11	0.992	3.22±0.07	0.995	3.39±0.07	0.998	3.08±0.32	0.982	2.53±0.06
	0.954	2.25±0.10	0.966	2.61±0.07	0.972	2.75±0.06	0.981	2.50±0.05	0.947	2.70±0.06
	0.906	2.13±0.11	0.923	2.52±0.07	0.931	2.69±0.06	0.946	2.56±0.06	0.894	2.92±0.07
	0.842	2.00±0.10	0.864	2.26±0.06	0.875	2.55±0.06	0.893	2.66±0.06	0.825	2.79±0.07
	0.765	1.79±0.10	0.791	2.41±0.07	0.804	2.55±0.06	0.825	2.68±0.06	0.745	2.34±0.06
	0.678	1.96±0.11	0.707	2.44±0.07	0.721	2.23±0.06	0.745	2.47±0.06	0.653	2.13±0.06
	0.579	1.89±0.11	0.613	2.43±0.07	0.628	2.26±0.06	0.655	2.37±0.06	0.553	1.56±0.06
	0.476	1.94±0.11	0.512	2.03±0.07	0.527	1.94±0.06	0.556	1.77±0.05	0.449	1.19±0.05
	0.368	1.73±0.11	0.407	1.84±0.07	0.423	1.60±0.06	0.452	1.41±0.05	0.331	0.74±0.04
	0.244	1.89±0.11	0.286	1.51±0.06	0.302	1.14±0.05	0.334	0.99±0.04	0.189	0.43±0.03
	0.099	1.66±0.10	0.141	1.15±0.05	0.160	0.87±0.04	0.193	0.76±0.04	0.033	0.27±0.03
	−0.059	1.31±0.08	−0.016	0.80±0.04	0.003	0.52±0.03	0.037	0.47±0.03	−0.143	0.22±0.02
	−0.239	0.94±0.07	−0.193	0.69±0.04	−0.172	0.35±0.03	−0.139	0.33±0.02	−0.329	0.10±0.02
	−0.429	0.52±0.05	−0.381	0.23±0.03	−0.358	0.13±0.02	−0.326	0.12±0.02	−0.514	0.12±0.02
	−0.616	0.26±0.05	−0.566	0.17±0.03	−0.545	0.08±0.02	−0.512	0.13±0.02	−0.688	0.09±0.02
							−0.690	0.16±0.02		
σ_{CEX}(mb)	15.8±0.3±1.2		14.3±0.1±1.1		12.1±0.1±1.1		11.4±0.1±1.0		10.1±0.1±0.8	

III. Figure 13 shows our results together with the high-statistics data of Alston-Garnjost *et al.*[38] As can be seen from this figure, our results are consistent with those of Alston-Garnjost *et al.*[38]

B. Comparison with potential models

Here we compare our differential-cross-section results with the predictions of the following $\bar{N}N$ potential models: Paris model,[3] Nijmegen model,[4] Dover-Richard[2] models I and II, and boundary-condition (black-sphere annihilation) model.[39] All these models are based on G-parity transformed one-boson-exchange potentials for the NN interactions. However, it is well known that the $\bar{N}N$ potential constructed in this way is valid only for the long-range part ($r \gtrsim 1$ fm) of the $\bar{N}N$ interactions. The

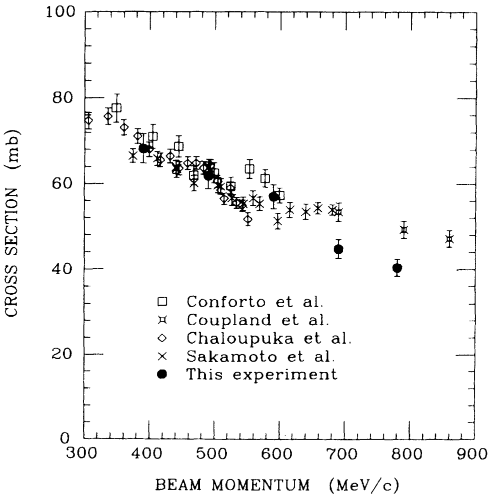

FIG. 12. The total elastic cross section as a function of incident momentum is compared with the previous results.

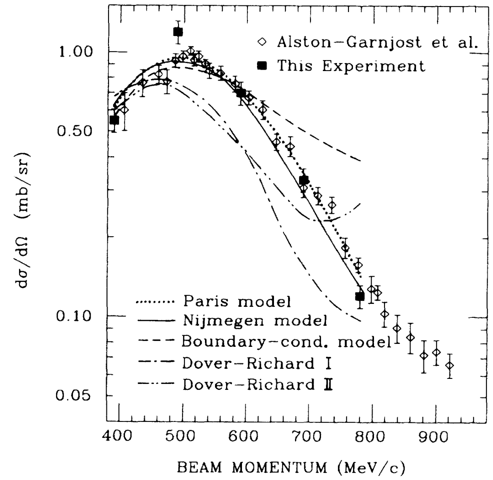

FIG. 13. Backward elastic differential cross section as a function of incident momentum. Our results are compared with those of Alston-Garnjost *et al.* (Ref. 38). Solid curves, Nijmegen model (Ref. 4); dashed curves, boundary-condition model (Ref. 39); dotted curves, Paris model (Ref. 3); dotted-dashed curves, Dover-Richard model (Ref. 2) I; double-dotted-dashed curves, Dover-Richard model (Ref. 2) II.

short-range part of the *NN* interactions is usually treated phenomenologically, and we do not know how to transform this phenomenological short-range part to obtain the corresponding $\bar{N}N$ potential. Moreover, the annihilation mechanism dominates in the short-range $\bar{N}N$ interactions, which does not exist in the *NN* interactions. In order to construct the full $\bar{N}N$ potential, a variety of prescriptions are taken to represent the annihilation potential. This brings about significant differences among $\bar{N}N$ potential models even though original meson-exchange potentials all fit *NN* data. New $\bar{N}N$ data with good quality then serve to test the validity of various potential models. It should be noted here that the clear difference among the models would show up in those features of the data which are sensitive to the short-range behavior of the $\bar{N}N$ interactions. For a significant test of meson-exchange part of the potential (i.e., a test of the original *NN* potential), perhaps one should call for spin observables which are sensitive to the small differences in the amplitudes.

Before proceeding to the comparison of the data with the predictions of various potential models, let us briefly summarize how these models are constructed. Dover and Richard[2] start with the *G*-parity transformed Paris *NN* potential[40] with a square-well cutoff, supplemented with a phenomenological short-range potential with the same shape for the real and imaginary parts (three parameters for model I and four parameters for model II). The Paris model[3] uses the same meson-exchange part of the $\bar{N}N$ potential as used by Dover and Richard, i.e., the *G*-parity-transformed Paris *NN* potential,[40] but with a phenomenological short-range real part (three parameters) and a short-range, state- and energy-dependent imaginary part (12 parameters). The Nijmegen model[4] makes a coupled-channel approach to construct the $\bar{N}N$ potential. For the diagonal part of the $\bar{N}N$ potential, this model uses the *G*-parity transformed Nijmegen-*D* *NN* potential[41] with a modification of the cutoff in the inner region, added with a phenomenological short-range part (eight parameters). The off-diagonal short-range annihilation potential is parametrized by four parameters. In the boundary-condition-model calculation of Mizutani *et al.*,[39] the *G*-parity-transformed Bryan-Scott one-boson-exchange *NN* potential[42] with a cutoff mass $\Lambda = 980$ MeV was used with an annihilation radius of $r_a = 0.5$ fm (one parameter). This annihilation radius was chosen to best reproduce the present $\bar{p}p$ elastic-scattering results together with our $\bar{p}p$ charge-exchange results.[20]

Our elastic differential-cross-section data are compared with the predictions of the potential models in Fig. 14. Also the backward differential cross section is compared with the predictions of these models in Fig. 13, where it is observed that the Paris[3] and Nijmegen[4] models give a nice account of the $\bar{p}p$ backward data. However, this does not necessarily mean the excellence of the models, simply because the backward elastic data of Alston-Garnjost *et al.*[38] were fitted to determine the free parameters involved in these models. The results of the Dover-

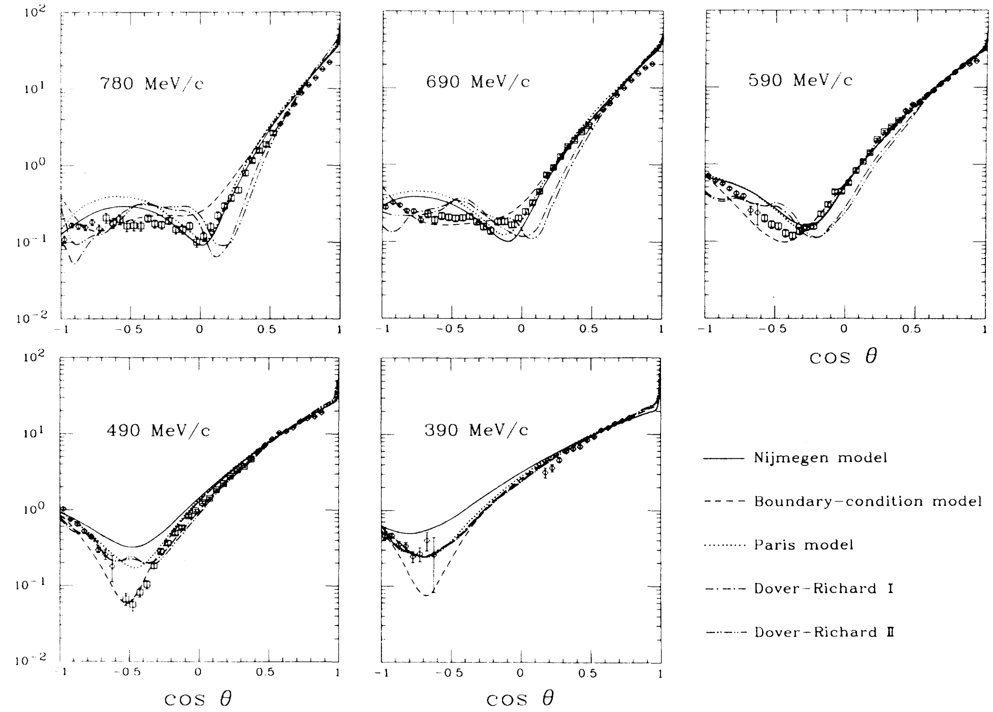

FIG. 14. Our $\bar{p}p$ elastic differential cross sections are compared with some theoretical predictions. Solid curves, Nijmegen model (Ref. 4); dashed curves, boundary-condition model (Ref. 39); dotted curves, Paris model (Ref. 3); dotted-dashed curves, Dover-Richard model (Ref. 2) I; double-dotted-dashed curves, Dover-Richard model (Ref. 2) II.

Richard[2] models I and II strongly deviate from the data, but it should be noted that the backward elastic data were not fitted to determine the free parameters of these models. The boundary-condition model[39] can reproduce the backward elastic data below ~ 600 MeV/c, but it predicts too large a backward differential cross section at higher momenta.

The global behavior of the theoretically calculated elastic differential cross sections shown in Fig. 14 indicates that none of the models can completely explain the data. The Paris and Nijmegen models show similar behavior at all momenta, though the Nijmegen model exhibits a shallower diffraction minimum below 490 MeV/c. Both models give rather smooth backward angular distributions, while the data seem to indicate a more complicated backward structure above 690 MeV/c. The Dover-Richard models I and II both show oscillatory behavior at backward angles and a faster falloff than the other models in the angular region of $0 \lesssim \cos\theta \lesssim 0.5$. The boundary-condition model reproduces the data rather well at 490 and 590 MeV/c, but its prediction of the backward angular distribution starts to deviate from the data above 690 MeV/c. It is also interesting to note that the boundary-condition model can reproduce the deep diffraction minimum observed at 490 MeV/c.

In Fig. 15 we also compare our $\bar{p}p$ charge-exchange data[20] with the theoretical calculations with the $\bar{N}N$ potential models discussed above. Our charge-exchange data are characterized by a sharp spike followed by a dip-bump structure in the forward direction. However, as the beam momentum lowers the position of the dip moves to larger angles and the depth of the dip seems to become shallower. The recent $\bar{p}p$ charge-exchange results reported by Brückner *et al.*[43] show a forward peaking followed by a smooth falloff at 287 and 183 MeV/c. Their data at 590 MeV/c seem to be consistent with our data.[20]

All theoretical calculations show the existence of the forward dip as seen in Fig. 15. The Nijmegen model and the boundary-condition model rather well reproduce the behavior of the forward dip as a function of beam momentum as indicated by the experimental data. However, the Paris model badly fails to predict the depth of the dip: it gives too deep a structure at all experimentally investigated beam momenta. The Dover-Richard models I and II also predict too deep a structure below 600 MeV/c, although at higher momenta they predict better forward behavior.

According to Mizutani *et al.*,[39] the backward structure observed in $\bar{p}p$ elastic scattering above 690 MeV/c is mainly due to the annihilation potential, since without the annihilation potential the $\bar{p}p$ elastic angular distributions calculated with meson-exchange potentials show backward peaking. The large-angle behavior of the $\bar{p}p$ elastic angular distributions calculated with the Dover-Richard models I and II is probably connected with their strong annihilation potentials. In this regard, the $\bar{p}p$ backward elastic scattering provides information on the $\bar{N}N$ annihilation potential as noted by Mizutani *et al.*[39]

The forward dip-bump structure in the $\bar{p}p \to \bar{n}n$ reaction may also be sensitive to the $\bar{N}N$ short-range dynamics. It is qualitatively explained[44] as due to the interference of the pion-exchange amplitude which is dominant in

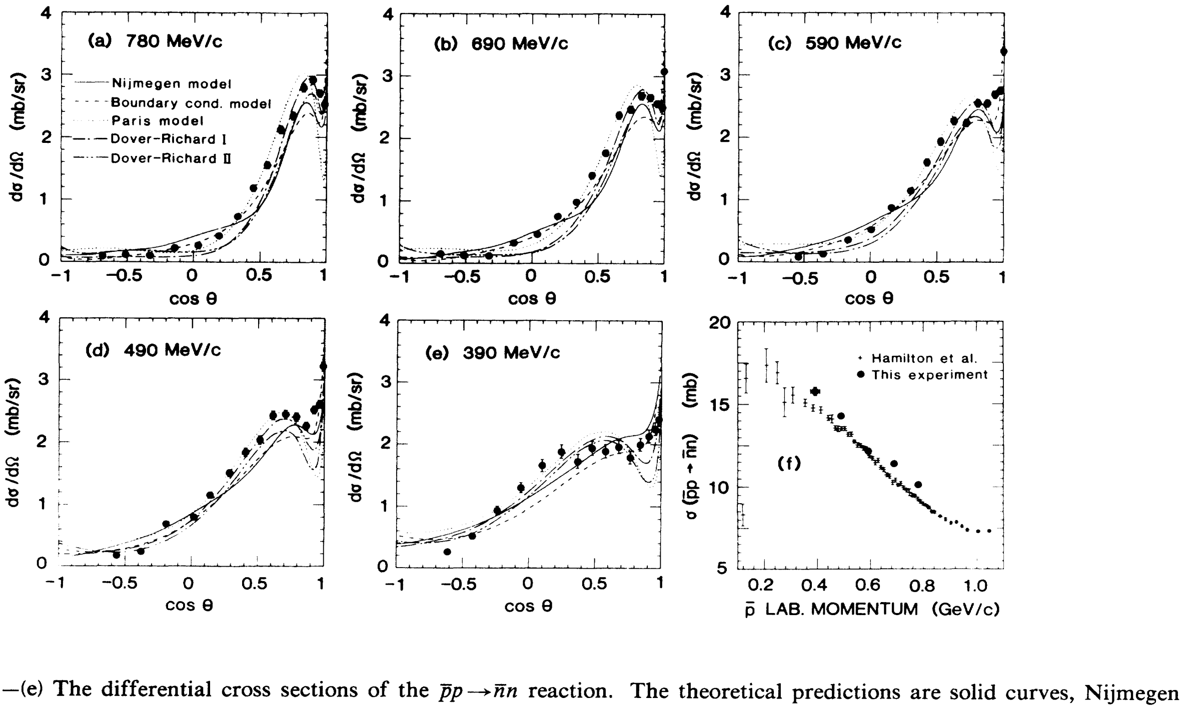

FIG. 15. (a)—(e) The differential cross sections of the $\bar{p}p \to \bar{n}n$ reaction. The theoretical predictions are solid curves, Nijmegen model (Ref. 4); dashed curves, boundary-condition model (Ref. 39); dotted curves, Paris model (Ref. 3); dotted-dashed curves, Dover-Richard model (Ref. 2) I; double-dotted-dashed curves, Dover-Richard model (Ref. 2) II. (f) The integrated charge-exchange cross-section data are compared with the data of Hamilton *et al.* (Ref. 42).

the low-momentum-transfer region with a coherent "background amplitude." From the momentum-dependence of the position of the dip observed in our $\bar{p}p \rightarrow \bar{n}n$ data,[20] Dover considers[45] that this background amplitude is a manifestation of the short-range dynamics because of its lack of significant t dependence, and, in particular, that it is related to the annihilation potential. On the other hand, Mizutani *et al.*[39] quantitatively studied the contribution of each helicity amplitude in $\overline{N}N$ scattering. They found that the forward dip-bump structure in the $\bar{p}p \rightarrow \bar{n}n$ reaction is due to an interference between the rapidly decreasing $|\phi_2|^2 = |\langle ++|--\rangle|^2$ and increasing $|\phi_4|^2 = |\langle +-|-+\rangle|^2$ and $|\phi_5|^2 = |\langle ++|+-\rangle|^2$. They also found that in the forward direction of the $\bar{p}p \rightarrow \bar{n}n$ reaction, ϕ_2 and ϕ_4 are dominant, but $\phi_1 = \langle ++|++\rangle$ and $\phi_3 = \langle +-|+-\rangle$ cannot be negligible in the dip-bump region. In fact, if ϕ_1 and ϕ_3 are too small in the forward direction the dip-bump structure appears to be quite pronounced, and this is the reason why the Paris meson-exchange potential[40] badly fails to reproduce the $\bar{p}p \rightarrow \bar{n}n$ forward structure.[39] Mizutani *et al.*[39] also note that the $\bar{p}p \rightarrow \bar{n}n$ dip-bump structure is sensitive to the short-range cutoff procedure of the Nijmegen potential.

To conclude this section, we point out that the boundary-condition model[39] gives fairly good account of both $\bar{p}p \rightarrow \bar{p}p$ and $\bar{p}p \rightarrow \bar{n}n$ data as a whole, although some modification is definitely needed to improve the $\bar{p}p \rightarrow \bar{p}p$ backward behavior above 690 MeV/c. It is remarkable that a model with a minimum number of free parameters can do as well as any other more complicated models in describing the main aspects of the $\overline{N}N$ interactions. This strongly suggests that the angular distributions of the $\bar{p}p \rightarrow \bar{p}p$ and $\bar{p}p \rightarrow \bar{n}n$ reactions are mainly determined by the purely geometrical aspects.

V. CONCLUSIONS

We have presented the differential cross sections of $\bar{p}p$ elastic scattering at five incident beam momenta, 390, 490, 590, 690, and 780 MeV/c. Our data agree with the previous results with some exceptions. At 690 and 780 MeV/c, our forward differential cross sections and total elastic cross sections are lower than those of Eisenhandler *et al.*[15] by 10–20%. The differential cross sections at $\theta = 180°$ deduced from our data agree with the high-statistics data of Alston-Garnjost *et al.*[38]

We have compared our results with the predictions of various $\overline{N}N$ potential models.[2–4,39] None of the theoretical models considered can completely explain the present $\bar{p}p$ elastic results in the full momentum range investigated. In particular, the structure in the backward angles above 690 MeV/c cannot be reproduced with these models. Since this backward structure is reported to be sensitive to the $\overline{N}N$ annihilation potential,[39] our data should provide useful constraints on the investigation of the $\overline{N}N$ annihilation potential.

We have also compared our $\bar{p}p$ charge-exchange results[20] with the predictions of the same $\overline{N}N$ potential models[2–4,39] as compared with the elastic results. Here, the characteristic dip-bump structure in the forward direction is reproduced rather well by the Nijmegen model[4] and the boundary-condition model.[39] On the other hand, the Paris model[3] shows a too pronounced forward dip-bump structure. The Dover-Richard models[2] I and II, which use the same Paris NN potential[40] as used by the Paris model,[3] also show the same tendency, though less pronounced.

From these comparisons, it appears that the boundary-condition model[39] with only one free parameter reproduces rather well both $\bar{p}p$ elastic and charge-exchange data as a whole. At least it can do as well as or better than other more complicated models which have much more free parameters. This suggests that the dominant features of the $\bar{p}p$ elastic and charge-exchange angular distributions are determined by the geometrical aspects.

In conclusion, it is highly desirable to make a reanalysis of the $\overline{N}N$ potential models proposed so far, including new $\overline{N}N$ scattering data in the fits to determine the parameters involved in the models.

ACKNOWLEDGMENTS

We would like to gratefully acknowledge the excellent machine operation of the staff of KEK accelerator department and the help of the staff of KEK experiment supporting group. Thanks are also due to Mr. Y. Umeda who participated in the early phase of this experiment. We wish to thank the following people for sending us the results of theoretical calculations: Dr. T. Mizutani and Dr. R. Tegen, the boundary-condition model; Dr. M. Lacombe, the Paris model; Dr. P. Timmers, the Nijmegen model; and Dr. J. M. Richard, the Dover-Richard model. One of us (K.N.) is grateful to Dr. T. Mizutani for enlightening discussions.

APPENDIX: RESULTS OF THE $\bar{p}p \rightarrow \bar{n}n$ REACTION

For completeness, we summarize in Table IV the differential cross sections and the integrated cross sections of the charge-exchange reaction, $\bar{p}p \rightarrow \bar{n}n$, which has been measured[20] in the present experiment concurrently with $\bar{p}p$ elastic scattering. In Table IV, the errors associated with the differential cross sections are statistical only, and the systematic errors for the differential cross sections are given in the second line. The first errors associated with the charge-exchange cross sections (σ_{CEX}) are statistical, and the second errors are systematic. To deduce the integrated charge-exchange cross sections σ_{CEX}, the corrections for the unmeasured backward differential cross sections were assumed to be given by the theoretical calculations by Mizutani *et al.*[39] These corrections are only less than 5%, and the ambiguities in the corrections are taken into account in the systematic errors associated with σ_{CEX}.

Figures 15(a)–(e) show the differential-cross-section results compared with some theoretical calculations and Fig. 15(f) shows σ_{CEX} compared with the high-statistics results of Hamilton *et al.*[46] These figures are reproduced from Ref. 20, but the differential-cross-section curves calculated with the Dover-Richard optical potential model[2] are added.

[*] Present address: National Laboratory for High Energy Physics, Oho, Ibaraki 305, Japan.

[†] Present address: Department of Physics, Kobe University, Kobe 657, Japan.

[‡] Present address: Rutherford-Appleton Laboratory, Chilton, Didcot, Oxon, UK.

[§] Present address: Computer Engineering Division, NEC Corporation, Fuchu-shi, Tokyo 183, Japan.

[1] R. A. Bryan and R. J. N. Phillips, Nucl. Phys. **B5**, 201 (1968); **B7**, 481(E) (1968).

[2] C. B. Dover and J. M. Richard, Phys. Rev. C **21**, 1466 (1980).

[3] J. Côté *et al.*, Phys. Rev. Lett. **48**, 1319 (1982).

[4] P. H. Timmers *et al.*, Phys. Rev. D **29**, 1928 (1984).

[5] M. Kohno and W. Weise, Nucl. Phys. **A454**, 429 (1986).

[6] O. D. Dalkarov and F. Myhrer, Nuovo Cimento, **40A**, 152 (1977).

[7] A. M. Green, J. A. Niskanen, and J. M. Richard, Phys. Lett. **121B**, 101 (1983).

[8] A. M. Green and J. A. Niskanen, Nucl. Phys. **A412**, 448 (1984).

[9] M. Maruyama and T. Ueda, Nucl. Phys. **A364**, 297 (1981).

[10] R. A. Freedman, W-Y. P. Hwang, and L. Wilets, Phys. Rev. D **23**, 1103 (1981).

[11] M. A. Alberg *et al.*, Phys. Rev. D **27**, 536 (1983).

[12] A. Faessler, G. Lübeck, and K. Shimizu, Phys. Rev. D **26**, 3280 (1982).

[13] S. Furui and A. Faessler, Nucl. Phys. **A424**, 525 (1984).

[14] R. Tegen, T. Mizutani, and F. Myhrer, Phys. Rev. D **32**, 1672 (1985); R. Tegen, F. Myhrer, and T. Mizutani, report, 1985 (unpublished).

[15] E. Eisenhandler *et al.*, Nucl. Phys. **B113**, 1 (1976).

[16] W. Brückner *et al.*, Phys. Lett. **166B**, 113 (1986).

[17] B. Conforto *et al.*, Nuovo Cimento **54A**, 441 (1968).

[18] S. Sakamoto *et al.*, Nucl. Phys. **B195**, 1 (1982).

[19] Preliminary results have been reported by K. Nakamura and T. Tanimori, in *Antiproton 1984,* edited by M. R. Pennington (Adam Hilger, Bristol, 1985), p. 329.

[20] K. Nakamura *et al.*, Phys. Rev. Lett. **53**, 885 (1984).

[21] T. Tanimori *et al.*, Phys. Rev. Lett. **55**, 1835 (1985).

[22] T. Kageyama *et al.*, Jpn. J. Appl. Phys. **24**, 1522 (1985).

[23] T. Sumiyoshi, S. Suzuki, and K. Nakamura, Jpn. J. Appl. Phys. **22**, 1606 (1983).

[24] T. Tanimori *et al.*, Nucl. Instrum. Methods **216**, 57 (1983).

[25] T. Fujii *et al.*, Nucl. Instrum. Methods **215**, 357 (1983).

[26] H. Wind, Nucl. Instrum. Methods **115**, 431 (1974).

[27] D. G. Cassel and H. Kowalski, Nucl. Instrum. Methods **185**, 235 (1981).

[28] D. I. Lowenstein *et al.*, Phys. Rev. D **23**, 2788 (1981).

[29] J. G. Loken and M. Derrick, Phys. Lett. **3**, 334 (1963).

[30] K. Nakamura *et al.*, Phys. Rev. Lett. **52**, 731 (1984).

[31] M. R. Clover *et al.*, Phys. Rev. C **26**, 2138 (1982).

[32] M. Cahay *et al.*, Phys. Lett. **115B**, 7 (1982).

[33] M. Cahay *et al.*, Nucl. Phys. **A393**, 237 (1983).

[34] A. S. Iljinov *et al.*, Nucl. Phys. **A382**, 378 (1982).

[35] D. Garreta *et al.*, Phys. Lett. **150B**, 95 (1985).

[36] V. Chaloupka *et al.*, Phys. Lett. **61B**, 487 (1976).

[37] M. Coupland *et al.*, Phys. Lett. **71B**, 460 (1977).

[38] M. Alston-Garnjost *et al.*, Phys. Rev. Lett. **43**, 1901 (1979).

[39] T. Mizutani, F. Myhrer, and R. Tegen, Phys. Rev. D **32**, 1663 (1985); (private communication).

[40] M. Lacombe *et al.*, Phys. Rev. C **21**, 861 (1980).

[41] M. M. Nagels, T. A. Rijken, and J. J. de Swart, Phys. Rev. D **12**, 744 (1975).

[42] R. A. Bryan and B. L. Scott, Phys. Rev. **177**, 1435 (1969).

[43] W. Brückner *et al.*, Phys. Lett. **169B**, 302 (1986).

[44] E. Leader, Phys. Lett. **60B**, 290 (1976).

[45] C. B. Dover, in *Proceedings of the Second Conference on the Intersection between Particle and Nuclear Physics,* Lake Louise, Canada, 1986, edited by D. Geesaman (AIP Conf. Proc. No. 150) (AIP, New York, 1986).

[46] R. P. Hamilton *et al.*, Phys. Rev. Lett. **44**, 1179 (1980).